COMMUNICATION

Check for updates

Detection of wavelength in the range from ultraviolet to near infrared light using two parallel PtSe₂/thin Si Schottky junctions†

Wen-Hua Yang,[a] Xin-Yuan Jiang,[a] Yu-Tian Xiao,[a] Can Fu,[a] Jian-Kun Wan,[a] Xiang Yin,[a] Xiao-Wei Tong,[a] Di Wu, [ID][b] Li-Miao Chen [ID][c] and Lin-Bao Luo [ID]*[a]

A wavelength sensor as a representative optoelectronic device plays an important role in many fields including visible light communication, medical diagnosis, and image recognition. In this study, a wavelength-sensitive detector with a new operation mechanism was reported. The as-proposed wavelength sensor which is composed of two parallel PtSe₂/thin Si Schottky junction photodetectors is capable of distinguishing wavelength in the range from ultraviolet to near infrared (UV-NIR) light (265 to 1050 nm), in that the relationship between the photocurrent ratio of both photodetectors and incident wavelength can be numerically described by a monotonic function. The unique operation mechanism of the thin Si based wavelength sensor was unveiled by theoretical simulation based on Synopsys Sentaurus Technology Computer Aided Design (TCAD). Remarkably, the wavelength sensor has an average absolute error of ±4.05 nm and an average relative error less than ±0.56%, which are much better than previously reported devices. What is more, extensive analysis was performed to reveal how and to what extent the working temperature and incident light intensity, and the thickness of the PtSe₂ layer will influence the performance of the wavelength sensor.

New concepts

In this manuscript, we proposed a new wavelength sensor based on two identical PtSe₂/thin Si Schottky junctions that are able to distinguish wavelengths in the range of UV-NIR (265–1050 nm). Device performance analysis revealed that the two parallel heterojunction photodetectors actually exhibit completely different spectrum responses under identical illumination conditions, which empowers the whole device to quantitatively determine the wavelength as the relationship between the photocurrent ratio and incident wavelength actually follows a typical monotonic function in the range from 265 to 1050 nm. The operation of the wavelength sensor is related to not only the wavelength dependent photo-absorption rate but also the thin thickness of the Si wafer. Further device analysis reveals that the wavelength sensor has an average absolute error of less than ±4.05 nm, and the average relative error is less than ±0.56%, which is much better than the previously reported results. These results along with the simple device geometry suggest that the current wavelength sensor made of two parallel PtSe₂/thin Si Schottky junctions is of potential importance in future wavelength sensing devices and systems.

Introduction

High-performance wavelength sensors (also called color detector, spectrum recognition device) that are capable of distinguishing wavelength quantitatively have important applications in many scientific and industrial fields, such as

artificial intelligence assisted driving, image sensing, optical communication, medical diagnosis, space and safety detection, *etc.*[1–5] For example, in the field of traffic safety, a receiver sensor can detect the wavelength of traffic lights to realize a robust communication for short to medium distance, which is of vital significance to traffic safety.[6] In addition, for color blind patients, light information can be collected by the color sensor and converted into the corresponding RGB (red, green and blue) value using a micro-controller, then displayed on the light emitting diode (LED), which helps color blind patients to precisely distinguish different colors.[7]

In light of the above promising application, significant efforts have been devoted to developing various wavelength sensors with different operating mechanisms. To date, wavelength detection can be realized by using either filter-assisted[8–11] or filter-free technology.[12–16] Take the filter-assisted technology for example; a wavelength sensor composed of photodetectors is able to determine the relative proportions of red, green and blue

[a] *School of Electronic Science and Applied Physics, Hefei University of Technology, Hefei, 230009, China. E-mail: luolb@hfut.edu.cn*

[b] *Key Laboratory of Materials Physics of Ministry of Education, Department of Physics and Engineering, Zhengzhou University, Zhengzhou 450052, China*

[c] *Hunan Provincial Key Laboratory of Micro & Nano Materials Interface Science, College of Chemistry and Chemical Engineering, Central South University, Changsha, 410083, China*

† Electronic supplementary information (ESI) available. See DOI: 10.1039/d1mh00286d

(RGB) light separated by the filters, and then convert the RGB values into the wavelength by referring to the CIE (International Commission on Illumination) 1931 color space. Cong *et al.* successfully developed a color detector using a 40 nm standard complementary metal oxide semiconductor (CMOS) device, which consists of a two-dimensional (2D) polysilicon subwavelength grating as a filter and a CMOS photodiode to detect the three primary colors (*e.g.* RGB).[17] While this approach indeed proves to be reliable for wavelength determination, it, however, suffers from a relatively narrow detection range (400–700 nm) and relatively high cost due to the complicated device manufacturing process.[18] Moreover, the loss of photons because of absorption or reflection at the interface between the filter and the detector can limit the detection efficiency.[19–22] As an alternative to the traditional filter-assisted device, a filter-free color detector mainly relies on multiple p–n junctions or narrowband semiconductors to realize color discrimination.[23,24] Polzer *et al.* have reported a filter-less bipolar CMOS RGB color sensor for wavelength detection in the wavelength range from 400 to 900 nm. The detector was composed of three silicon photodiodes: a deep diode used as the sensing element for red light, a middle diode to detect green light and a shallow diode as the blue light detector.[25] Even though the fabrication of the filter-free device is compatible with the Si technology, this kind of device has a very complicated device configuration, which is unfavorable for practical application. In addition, the wavelength resolution of the wavelength detector is about tens of nanometers, which is far from satisfactory. Therefore, it is very urgent to propose a high-performance wavelength detector with good sensing resolution and broadband detection range.

Herein, we proposed a new wavelength sensor based on two identical PtSe$_2$/thin Si Schottky junctions that are able to distinguish wavelengths in the range of UV-NIR (265–1050 nm). Device performance analysis revealed that the two parallel heterojunction photodetectors actually exhibit completely different spectrum responses under identical illumination conditions, which empowers the whole device to quantitatively determine the wavelength as the relationship between the photocurrent ratio and incident wavelength actually follows a typical monotonic function in the range from 265 to 1050 nm. The operation mechanism of this thin Si based wavelength sensor was interpreted by theoretical simulation based on TCAD. Remarkably, the average absolute error is around ±4.05 nm, and the average relative error is about ±0.56%, which is much better than previously reported results. These results along with the simple device geometry suggest that the current wavelength sensor made of two parallel PtSe$_2$/thin Si Schottky junctions is of potential importance in future wavelength sensing devices and systems.

Results and discussion

In this study, the wavelength sensor consists of two multi-layered PtSe$_2$/n-type thin Si heterojunctions (Fig. 1a) that are assembled by transferring PtSe$_2$ layers onto a thin Si wafer. The detailed fabrication procedure is illustrated in Fig. S1 (ESI†). After assembly, two identical PtSe$_2$/thin Si Schottky junction photodetectors were placed on a printed circuit board (PCB) in a vertically stacked manner (Fig. 1b). The scanning electron microscopy (SEM) image of the PtSe$_2$ nanofilm is shown in
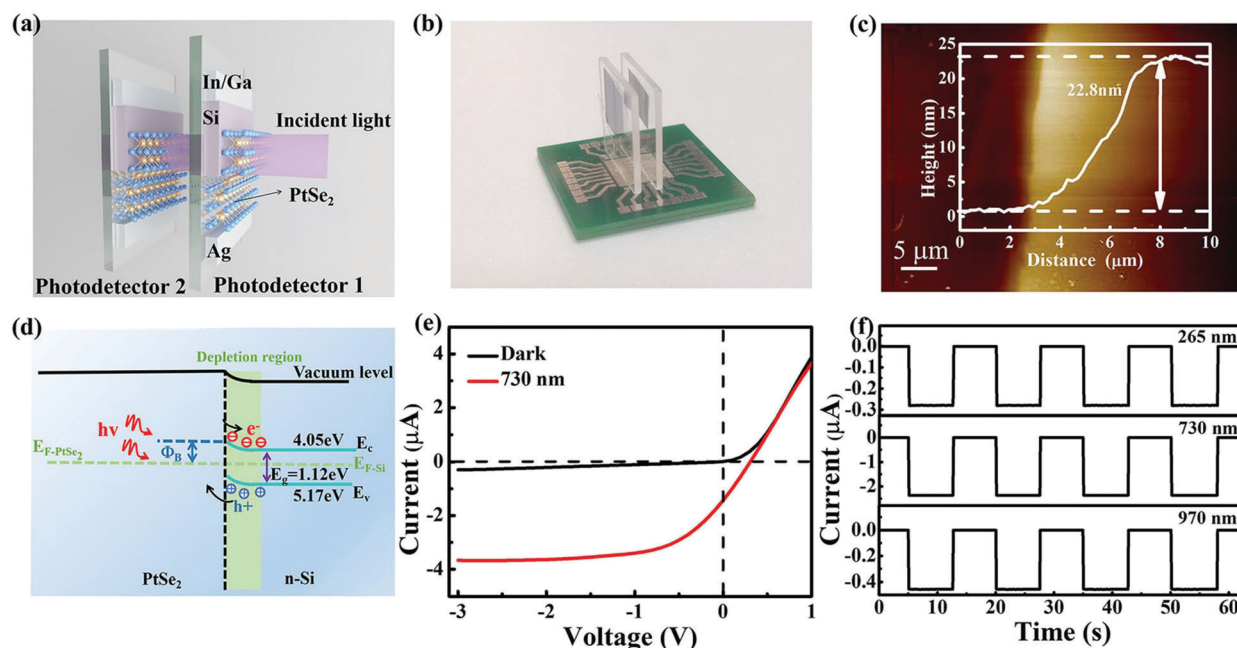
Fig. 1 (a) Schematic illustration of the PtSe$_2$/20 μm Si heterojunction wavelength sensor. (b) The digital picture of the wavelength sensor. (c) AFM image of the PtSe$_2$ layer; the inset shows the height profile. (d) Energy band diagram of the PtSe$_2$/thin Si heterojunction under light illumination at zero bias. (e) *I–V* characteristics of the heterojunction in the dark and under 730 nm light. (f) Photoresponse of the PtSe$_2$/20 μm Si Schottky junction to 265, 730 and 970 nm light illumination.

Fig. S2a (ESI†). It can be found that the PtSe$_2$ layer is a continuous and uniform film. The Raman spectrum in Fig. S2b (ESI†) reveals two prominent peaks at ∼179 and ∼208 cm^{-1}, which could be assigned to the E$_g$ in-plane vibrational mode of Se atoms within the layer and the A$_{1g}$ out-of-plane vibrational mode of Se atoms in opposite directions, respectively.[26–28] From the height distribution and marker lines shown in Fig. 1c, the PtSe$_2$ film has a thickness of ∼22.8 nm, according to which, the PtSe$_2$ layer can be regarded as a semi-metal.[29,30] Thereby the PtSe$_2$-thin Si contact is virtually a typical metal-semiconductor contact, whose energy band diagram at zero bias is shown in Fig. 1d. The work function of the PtSe$_2$ is located at ∼4.84 eV,[31] while the Fermi level (E_F) of n-Si with the resistivity of 1–10 Ω cm^{-1} is about 4.25 eV.[32] Electrons will diffuse from Si to PtSe$_2$, and holes are left within the depletion region in Si, leading to the formation of a built-in electric field at the PtSe$_2$/Si interface. Similar to other graphene/semiconductor heterojunctions,[33,34] upon illumination with a photon energy higher than the bandgap of Si (E_g = 1.12 eV), electron–hole pairs (EHPs) generated within or in the vicinity of the depletion region can be separated by the built-in electric field and collected by respective electrodes to form a photocurrent. Fig. 1e shows the current–voltage (I–V) curve of the PtSe$_2$/thin Si heterojunction in the dark and under 730 nm light illumination (100 μW cm^{-2}), respectively. Obviously, the heterojunction exhibited a photovoltaic property with an open-circuit voltage (V_{OC}) of about 0.25 V and a short-circuit current (I_{SC}) of about 1.52 μA. Based on these values, the PV power-conversion-efficiency, ideality factor and fill factors of the device are about 0.095%, 1.34 and 0.25, respectively. Although the power-conversion-efficiency and fill factors are relatively small, this relatively weak photovoltaic behavior can allow the PtSe$_2$/thin Si

heterojunction to work as a self-driven photodetector.[35] Further time-dependent photoresponse at zero bias indeed reveals that the device exhibits obvious sensitivity to incident light with good repeatability (Fig. 1f). Specifically, under 730 nm illuminations with a light intensity of 100 μW cm^{-2}, the I_{light}/I_{dark} is about 1.91 × 10^3. When the wavelength is replaced with 265 and 970 nm, the I_{light}/I_{dark} is much lower, even though the light intensities are the same (more performance analysis can be seen in Fig. S3, ESI†). This spectral selectivity is different from previously reported bulk Si based devices, whose peak sensitivity is often centered in NIR light region.[36,37]

Apart from the unique photoresponse, it is interesting to observe that when the two thin Si Schottky junction detectors were illuminated by different wavelengths of light, they displayed completely different spectral photoresponses. Fig. 2a plots the photoresponse in the range from UV to NIR. It can be easily observed that the first photodetector is characterized by a peak sensitivity at 730 nm, while the second one has a typical peak photoresponse at around 970 nm. What is more, the maximum photocurrent of the first photodetector is about 1.8 μA at 730 nm, which is much larger than that of the second one (41 nA@ 970 nm). By using the photocurrent values of both photodetectors, the responsivity (R) and specific detectivity (D^*) are estimated to be 207 mA W^{-1}, 4.75 × 10^{12} Jones for the first PtSe$_2$/thin Si Schottky photodetector, and 18.5 mA W^{-1}, 4.23 × 10^{11} Jones for the second one at zero bias voltage, respectively (Fig. 2b, the detailed calculation can be found in the ESI†). Understandably, the relatively smaller responsivity and specific detectivity of the second photodetector are due to the shadow effect of the first PtSe$_2$/thin Si heterojunction under light illumination. Fig. 2c plots the photocurrent ratio as a function of different incident
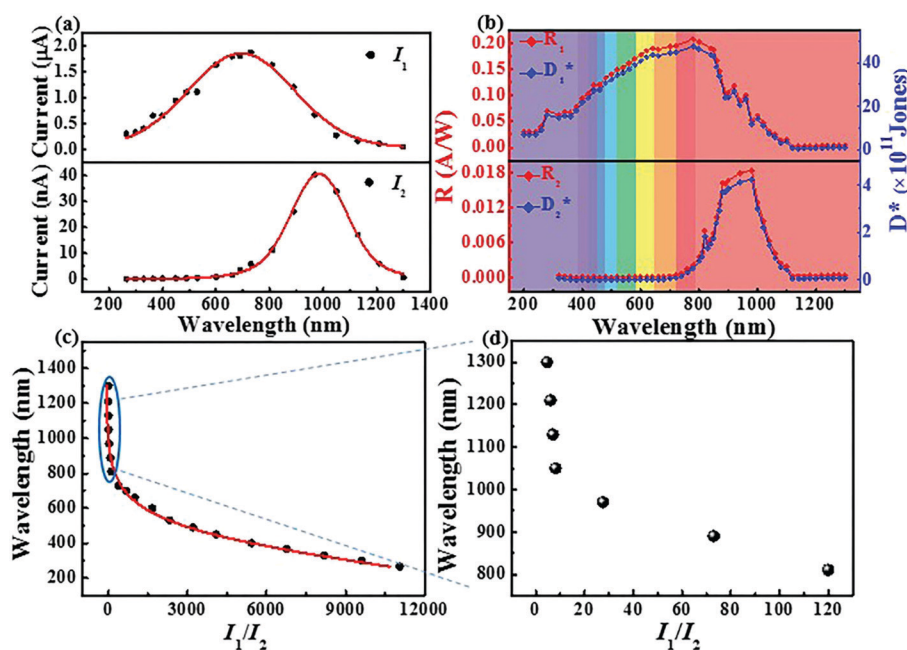

Fig. 2 (a) Photocurrent of the two Schottky junction photodetectors as a function of different wavelengths. (b) Photocurrent responsivity and specific detectivity of the two photodetectors as functions of different wavelengths. (c) The relationship between photocurrent ratio and the illumination wavelengths. (d) Accuracy test of the wavelength sensor.

wavelengths. It is very interesting to find that with the decrease in wavelength, the photocurrent ratio increases dramatically from 8.2 to nearly 1.1×10^4. Notably, the change in current ratio in the wavelength range from 1300 to 1050 nm is too inconspicuous to be observed (from 4.7 to 8.2, Fig. 2d), suggesting that the monotonic function is effective for the wavelength from 265 to 1050 nm.

To shed light on the above observation, Synopsys Sentaurus Technology Computer Aided Design (TCAD) simulation on the current of the two photodetectors was performed (in the simulation, the influence of the $PtSe_2$ has been taken into consideration according to its absorption spectrum (Fig. S4, ESI†)). It is seen that the current of the first photodetector increases initially and then decreases as the incident wavelength increases, and reaches a maximum value at about 730 nm (Fig. 3a). This is quite different from what was observed in the second photodetector, whose current is two orders of magnitude smaller than the first one when the wavelength is shorter than 730 nm. Moreover, the current begins to increase rapidly and starts to saturate when the wavelength is 970 nm. A further increase in wavelength, however, will lead to a decline in photocurrent. Such a discrepancy in photocurrent can lead to a monotonic decrease in photocurrent ratio (Fig. 3b), which is consistent with the above experimental results and is highly beneficial for the quantitative determination of wavelength. Further simulation results in Fig. 3c reveal that the above finding is due to the unique distribution of the photon absorption rate which is associated with wavelength dependent photoabsorption characteristics. Take the first photodetector for example, when the wavelength of the incident light is relatively short (e.g. at a wavelength of 265 nm), the penetration depth (photon absorption rate with relatively high value) of the

incident light is very shallow (less than 10 nm), suggesting that the photons are almost absorbed on the surface of the first heterojunction. However, as the incident light wavelength increases in the range of 265–730 nm, the penetration depth will gradually increase and even surpasses the whole thickness of the first photodetector at 730 nm. This finding is quite different from what was observed in the second photodetector that starts to absorb incident photons at 730 nm and reaches the strongest absorption at a wavelength of 970 nm. Thanks to the unique distribution of photon absorption rate, the two photodetectors display completely different optoelectronic characteristics. Fig. 3d illustrates EHPs under the illumination of short, medium and long wavelengths (e.g., 265, 730, and 970 nm). Under light illumination, the heterojunctions of both photodetectors can be divided into two regions: the depletion region (2 μm)[38] and diffusion region (316 μm for thin Si), both of which will contribute to the formation of photocurrent when EHPs are generated within this area. However, as the incident wavelength increases from 265 to 970 nm, the generation of EHPs will gradually extend from the first photodetector to the second one. Because of the thin thickness of the Si in comparison with the diffusion length, the majority of photo-induced EHPs will be separated by the built-in electric field, which is therefore responsible for the different photoresponse of both photodetectors.

The above result has indicated that the two thin Si photodetectors can help to determine the wavelength of incident light as the relationship between photocurrent ratio and wavelength follows a typical monotonic function. However, it is worth noting that the wavelength determination is subject to the influence of working temperature. Fig. 4a shows the variation of the photocurrent ratio at a working temperature of 5, 25 and
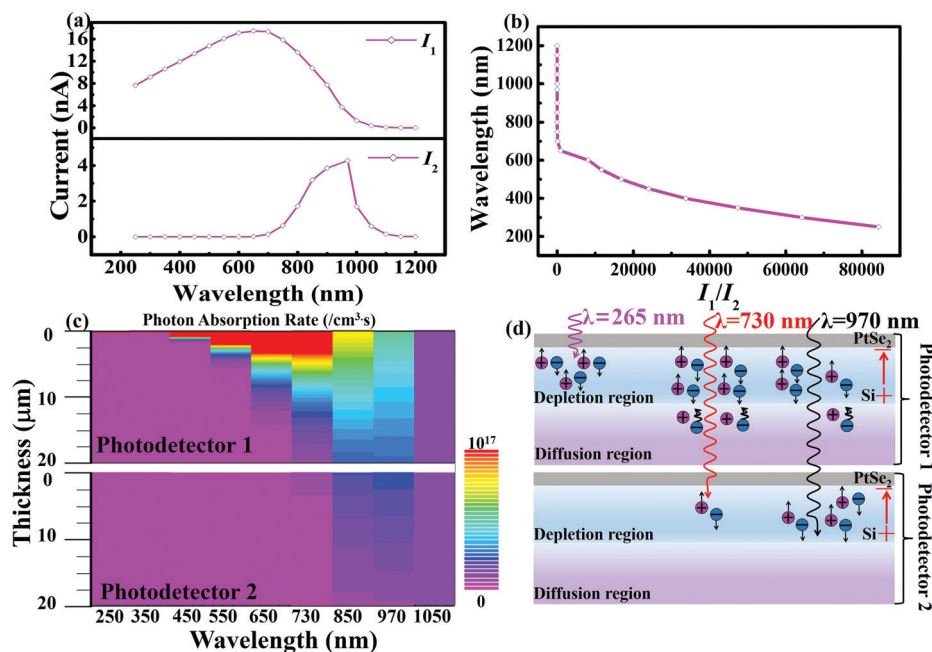

Fig. 3 (a) The current simulation results of the first and the second photodetector in the whole detection range. (b) The simulation of the photocurrent ratio of these two photodetectors. (c) The simulated photon absorption rate under different wavelengths of illumination. (d) Schematic diagram of carrier generation for the wavelength detector at different wavelengths.
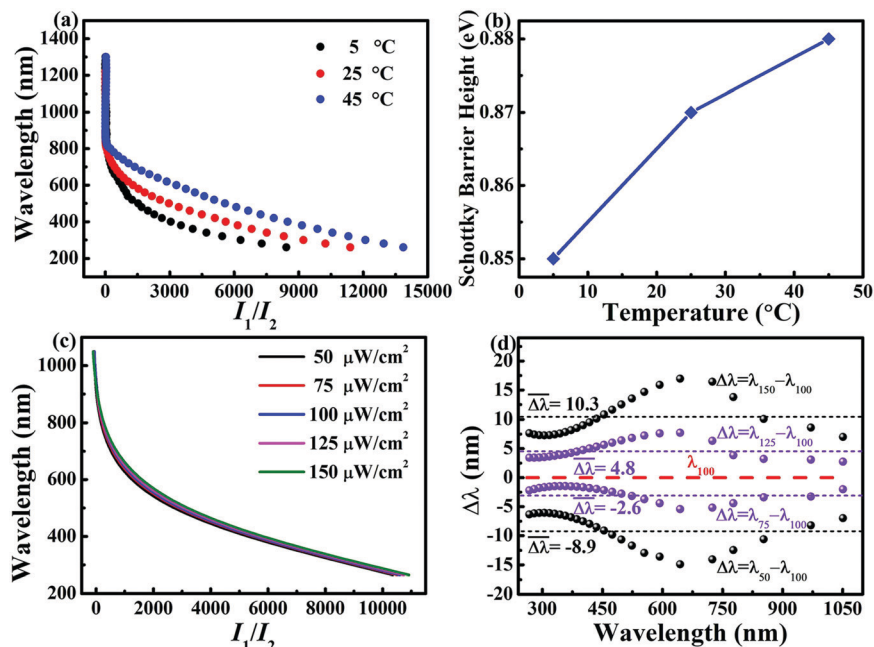
Fig. 4 (a) The wavelength of incident light varies with the photocurrent ratio of the two photodetectors at different temperatures. (b) Temperature-dependent Schottky barrier height. (c) The wavelength of incident light changes with the photocurrent ratio at different light intensities. (d) Error analysis of wavelength when the light intensity was changed by 50 μW cm^{-2}.

45 °C under ambient conditions. It can be found that relatively low working temperature can lead to a much smaller photocurrent ratio. Such temperature-dependent photocurrent is associated with the variation of barrier height of the PtSe$_2$/Si Schottky junction, which can be described by the thermionic emission theory of majority carriers over a zero bias barrier, as shown below:[39]

$$J_{s}(T) = A^{*}T^{2}\exp\left(-\frac{e\Phi_{BH}}{k_{B}T}\right) \qquad (1)$$

where J_s is the saturation current density, A^* is the effective Richardson constant, which is 252 A cm^{-2} K^{-2} for n-Si, e is the elementary charge, k_B is the Boltzmann constant, and T is the temperature. For temperatures at 5, 25 and 45 °C, the J_s is calculated to be 1.08×10^{-7}, 4.97×10^{-8} and $J_s = 3.55 \times 10^{-8}$ A cm^{-2}, respectively. Based on these values, the barrier height of the PtSe$_2$/thin Si Schottky junction is estimated to be 0.85, 0.87 and 0.88 eV, respectively, shown as Fig. 4b. This gradual increase in Schottky barrier height of the PtSe$_2$/thin Si device with increasing temperature leads to the strengthened built-in electric field at high temperature. As a result, the separation of the EHPs will be facilitated, which causes a relatively large photocurrent for both photodetectors. Note that although the strengthened electric field can facilitate the separation of EHPs, the extent of photocurrent enhancement for both photodetectors is quite different considering the fact that the generation of EHPs in the first photodetector is at least 2–3 orders of magnitude large than that of the second photodetector. Such a discrepancy in the density of EHPs will lead to slightly different evolution in photocurrent: for the second photodetector, when the built-in electric field was strengthened, the increase in photocurrent is very inconspicuous

as the majority of the EHPs have been separated at a low density of EHPs. However, it will be a different story for the first photodetector. Due to the relatively large density of EHPs, the slight enhancement in the electric field at high temperature will be very beneficial for high photocurrent as more EHPs will be efficiently separated prior to their recombination. Because of this reason, the photocurrent ratio of the present wavelength sensor increases with increasing temperature. Apart from temperature, the intensity of the incident light can influence the accuracy of the wavelength detection as well. Fig. 4c compares the photocurrent ratio-wavelength relationship when illuminated by light with various intensities (e.g., 50, 75, 100, 125, 150 μW cm^{-2}) at room temperature (25 °C), from which all five curves are close to each other. Further careful analysis of these curves reveals that the photocurrent ratio actually slightly increases with increasing light intensity. Such a slight increase in photocurrent ratio at relatively high light intensity inevitably causes a shift in wavelength determination. Fig. 4d compares the error distribution of wavelength when the light intensity was increased or decreased by 25 or 50 μW cm^{-2}, respectively. For convenience, the wavelength estimated at 100 μW cm^{-2} will be used as the reference standard. It can be seen that increase or decrease in light intensity by 50 μW cm^{-2} will bring about a relatively large shift in wavelength. Specifically, the maximum errors for the intensity of 150 and 50 μW cm^{-2} are estimated to be 16.9 nm and −14.9 nm at 645 nm, with an average error of 10.3 nm and −8.9 nm, respectively. This relatively large error can be eased by tuning the intensity by 25 μW cm^{-2}. In this case, the maximum errors for the intensity of 125 and 75 μW cm^{-2} are around 7.7 nm and −5.4 nm, with an average error of 4.8 nm and −2.6 nm, respectively, which is acceptable from the perspective of practical application. This result

demonstrates that the resolution of the present wavelength sensor is reliable as long as the light intensity is kept at an appropriate range.

Through the analyses of temperature and light intensity in Fig. 4a and c, the relationship between current ratio and light wavelength at different temperatures and light intensities can be expressed by the following empirical formula that is obtained by numerical fitting:

$$\lambda = A \ln\left(\frac{B}{\frac{I_1}{I_2} + C} - 1\right) + D \qquad (2)$$

where A, B, C and D are constants subject to the variation of detection temperature and light intensity. Detailed values of these four constants are provided in Table S1 (ESI†). Even though eqn (2) is a little complicated, it, however, can help us precisely calculate the wavelength once the temperature, light intensity and photocurrent ratio are known. Since in most cases, the wavelength sensing was carried out at room temperature, the numerical relationship between the light intensity, the photocurrent ratio and the wavelength of the incident light at 25 °C can be then simplified by a new expression as follows:

$$\lambda = \left(7.9e^{\frac{P}{120.2}} + 111\right) \ln\left(\frac{486.2e^{\frac{P}{69.3}} + 18515.9}{\frac{I_1}{I_2} + 175.9 - \frac{64.5}{\left(1 + \frac{P}{124.2}\right)^{95}}} - 1\right)$$
$$- 1.9e^{\frac{P}{54.7}} + 288.1$$
$$(3)$$

where P is the corresponding light intensity, and I_1/I_2 is the photocurrent ratio. Fig. 5 illustrates a curved face, through which the wavelengths under illumination with different light intensities can be easily estimated. Table 1 summarizes the absolute error and relative error between calculated wavelength (λ_{cal}) and actual wavelength (λ_{act}) under the light intensity of 125 μW cm^{-2}. It is obvious that for short-medium wavelength (<810 nm) illumination, the relative error is relatively small (normally less than ±0.6%), but for longer wavelengths (>900 nm), the corresponding deviation has a relatively large value (Normally larger than ±1.4%). Such an abnormal phenomenon at a longer wavelength is understandable as the photocurrent ratio is very small (less than twelve) in this region, and a slight change in photocurrent ratio can lead to a large error in comparison with that in the short wavelength region. In spite of this, we believe that both the absolute error and relative error in the long wavelength region could be relieved by choosing a more complicated fitting curve. The average absolute error (AAE) of the current wavelength sensor is estimated to be around ±4.05 nm, with a maximum value of −12.96 nm. Besides, the average relative error (ARE) is ±0.56%, with a maximum value of −1.44%, respectively. These values are much better than not only the wavelength sensor made of multiple Si
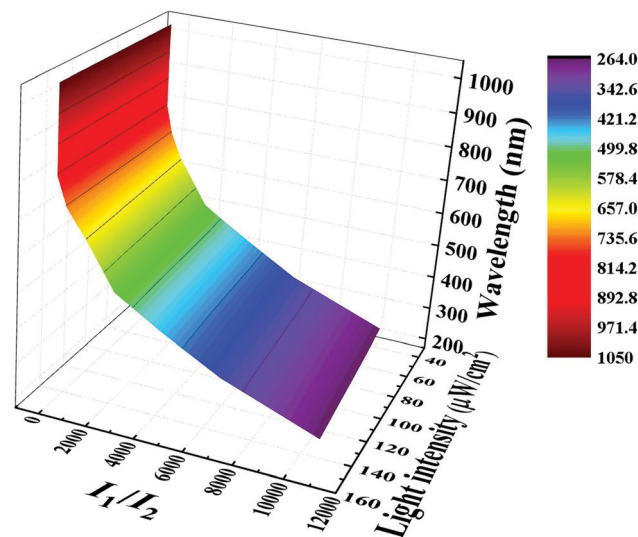

Fig. 5 The relationship between the photocurrent ratio and the wavelength of the incident light as a function of the light intensity.

Table 1 Analysis of the error between the calculated wavelength and the actual wavelength; the light intensity is around 125 μW cm^{-2}

Photocurrent ratio	λ_{act} (nm)	λ_{cal} (nm)	Absolute error (nm)	Relative error (%)
10757.45	265	264.09	−0.91	−0.34
2428.36	530	533.16	3.16	0.60
491.48	730	727.80	−2.20	−0.30
186.90	810	811.02	1.02	0.13
30.79	900	887.04	−12.96	−1.44
—	—	—	AAE = ±4.05	ARE = ±0.56

p–n photodiodes (the average relative error is ±2.5%),[40] but also the device composed of narrowband semiconductors (the absolute error is 80 nm).[23] and single CdS$_x$Se$_{1−x}$ nanowire alloy (the absolute error is 15 nm),[24] suggesting the great potential to replace the conventional wavelength sensors.

For the present wavelength sensor, the PtSe$_2$ layer actually acts as a transparent electrode in the device geometry: it can allow the penetration of the incident light from the first photodetector to the second one due to its relatively weak absorption capability. Meanwhile, it also forms a very effective Schottky junction with the thin Si, which will be helpful for the efficient separation of EHPs. Considering the fact that the properties of the two-dimensional materials are highly determined by its thickness,[41–44] other devices were also fabricated by using PtSe$_2$ layers with different thickness (e.g. 51.4 nm and 80.7 nm), so as to unveil how and to what extent the corresponding device performance will be influenced. It can be easily found that when the thickness of the PtSe$_2$ layer was increased to 51.4 and 80.7 nm, the corresponding photocurrents of both photodetectors will decrease by nearly 3–5 orders of magnitude (Fig. 6a) in comparison with that of the 22.8 nm PtSe$_2$ based device. This decay in photocurrent can be ascribed to the poor light transmittance at a relatively large thickness. Understandably, since the shadow effect of the thick and opaque PtSe$_2$ nanofilm can exert a direct
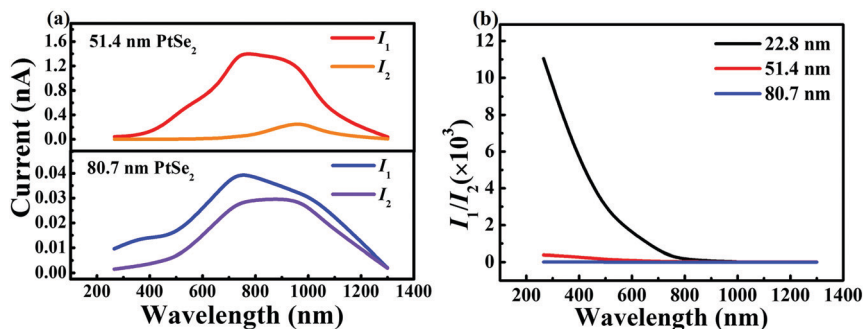
Fig. 6 (a) The photocurrent of the two photodetectors in the detection range when the thickness of $PtSe_2$ is 51.4 and 80.7 nm. (b) The corresponding photocurrent ratio for the wavelength sensor is composed of different thicknesses of the $PtSe_2$ layer.

effect on the first photodetector that is undoubtedly unprofitable to the photocurrent, the resultant photocurrent ratio decreases dramatically (Fig. 6b). On the other hand, although the $PtSe_2$ layer with thickness less than 20 nm is more transparent than the other thicker layer, it is however not suitable for device fabrication either in that the increase in light transmittance is achieved at the sacrifice of electrical conductivity ($PtSe_2$ layer with a thickness of 15 nm is composed of isolated nanoparticles, see Fig. S5, ESI†). Needless to say, this result suggests that $PtSe_2$ layers with thickness less or considerably larger than 20 nm are not suitable for wavelength sensor applications.

Experimental section

Material preparation and characterization

The $PtSe_2$ nanofilm was grown using a selenization approach. Briefly, a ~ 5 nm Pt film was deposited directly on a clean $SiO_2/$ Si substrate (300 nm SiO_2 thickness) *via* e-beam evaporation. The substrate was moved to the central area of the chemical vapor deposition furnace, and selenium (Se) powder (99.99% purity) was placed near the inlet of Ar/H_2 gas. The powder was then heated up to 220 °C to allow evaporation, and the evaporation gas was carried by using 60 SCCM Ar/H_2 gas flow. The temperature of the central zone of the furnace was maintained at ~ 450 °C. The morphology and topography of the $PtSe_2$ layer were studied by using an SEM instrument (JEOL Model JSM-6490) and AFM (Veeco NanoScope V). Raman spectra were recorded on a LabRAM HR Evolution (Horiba Jobin Yvon) equipped with a 532 nm argon-ion laser. Surface component analyses were performed using a monochromatic Al Kα source (1486.6 eV) produced by an XPS system.

Device fabrication and analysis

To fabricate the $PtSe_2$/thin Si heterojunction photodetector, 20 μm n-type Si wafer (resistivity: 1–7 Ω cm^{-1}) was first cut into small pieces with a size of 0.3 cm × 0.5 cm, and then etched in a diluted hydrofluoric acid solution for 5 minutes to remove the oxide layer on the surface. Then silicon samples were cleaned using acetone, ethanol, and deionized (DI) water for 5 minutes in turn and dried with nitrogen. Afterwards, the thin silicon was transferred to a glass substrate, followed by the

transfer of $PtSe_2$ film to the thin silicon surface. The $PtSe_2$ films were spin-coated with 5 wt% polymethylmethacrylate (PMMA) in chlorobenzene, and then the underlying SiO_2 on Si was removed in an 8 mol L^{-1} NaOH solution, followed by rinsing in deionized water to remove the remaining ions. The above thin Si was then soaked in deionized water solution, and slowly lifted to transfer the $PtSe_2$ films. Finally, a drop of Ag paste was placed at the $PtSe_2$ films, and the electrical contact for thin silicon was formed by attaching an In–Ga alloy onto the Si surface. After completion of a single photodetector fabrication, two identical photodetectors were placed in a parallel manner to form the wavelength detector. The electrical measurements of the device were performed using a semiconductor characterization system (4200-SCS, Keithley Co. Ltd). To study the spectral response, a lab-built optoelectronic system and monochromator (LE-SP-M300) were used. Meanwhile, light-emitting diodes as illumination sources (ThorLabs, collimated LEDs) were also employed to study the impact of different light intensities on the performance of the device. A power meter (Thorlabs GmbH., PM 100D) was employed to calibrate the light intensity of all light sources before measurement.

Theoretical simulation

TCAD software was adopted to simulate the photocurrent and photon absorption rate for two heterojunction photodetectors. The structure of the device was established using the two-dimensional process simulation module ATHENA in the TCAD software, and the size, the doping concentration and crystal orientation of the silicon substrate are defined by referring to the experimental result. In the ATLAS device simulator module, the light intensity and the position and angle of the incident light were defined to simulate the photoelectric behavior of the device and obtain the photocurrent and photon absorption rate of the devices. According to the simulated result, the Tonyplot (contours drawing component) was used to illustrate the spectra of the photon absorption rate in different colors.

Conclusions

In summary, a wavelength-sensitive detector made of two identical $PtSe_2$/20 μm Si heterojunctions was reported. The proposed

wavelength sensor can easily identify the wavelength of incident light in the range of UV to NIR (265–1050 nm), thanks to the relationship between the photocurrent ratio and incident wavelength following a typical bijection function. On the basis of the TCAD simulation, the operation of the wavelength sensor is related to not only the wavelength dependent photo-absorption rate but also the thin thickness of the Si wafer. Further device analysis reveals that the wavelength sensor has an average absolute error of less than ±4.05 nm, and the average relative error is less than ±0.56%. These results, along with the relatively simple fabrication process corroborate that the wavelength sensor is of potential importance in future wavelength sensing applications.

Author contributions

L. L. conceived the idea, supervised the research project, guided the experiments, and revised the paper. W. Y. and X. J. designed the experiments, prepared the samples, carried out the data collection, analysed the results and wrote the paper. Y. X., C. F., D. W. and X. T. simulated the device, helped to study the device performance, and assisted in analysing experimental data. J. W., X. Y. and L. C. assisted with the material characterization and searched for relevant references. All authors discussed the results and contributed to the manuscript.

Conflicts of interest

The authors declare that they have no competing interests.

Acknowledgements

Notes and references

1 W.-L. Tsai, C.-Y. Chen, Y.-T. Wen, L. Yang, Y.-L. Cheng and H.-W. Lin, *Adv. Mater.*, 2019, **31**, 1900231.
2 I. Dursun, C. Shen, M. R. Parida, J. Pan, S. P. Sarmah, D. Priante, N. Alyami, J. Liu, M. I. Saidaminov, M. S. Alias, A. L. Abdelhady, T. K. Ng, O. F. Mohammed, B. S. Ooi and O. M. Bakr, *ACS Photonics*, 2016, **3**, 1150–1156.
3 T.-K. Woodstock and R. F. Karlicek, *IEEE Sens. J.*, 2020, **20**, 12364–12373.
4 K. Liang, C.-W. Chow and Y. Liu, *Opt. Express*, 2016, **24**, 9383–9388.
5 D. Knipp, H. Stiebig, J. Folsch and H. Wagner, *J. Non-Cryst. Solids*, 1998, **227**, 1321–1325.
6 A.-M. Cailean, B. Cagneau, L. Chassagne, M. Dimian and V. Popa, *IEEE Sens. J.*, 2015, **15**, 4632–4639.
7 J. Mcdowell, *IEEE Potentials*, 2008, **27**, 34–39.
8 J. H. Han, D. Kim, T.-W. Lee, Y. Jeon, H. S. Lee and K. C. Choi, *ACS Photonics*, 2018, **5**, 3322.
9 J. Bao and M. G. Bawendi, *Nature*, 2015, **523**, 67.
10 A. Emadi, H. Wu, G. Graaf and R. Wolffenbuttel, *Opt. Express*, 2012, **20**, 489–507.
11 S.-W. Wang, C. Xia, X. Chen, W. Lu, M. Li, H. Wang, W. Zheng and T. Zhang, *Opt. Lett.*, 2007, **32**, 632–634.
12 S. H. Kong, D. D. L. Wijngaards and R. F. Wolffenbuttel, *Sens. Actuators, A*, 2001, **92**, 88–95.
13 M. P. Chrisp and B. Colo, *US Pat.*, 5880834, 1999.
14 G.-F. Dalla Betta, N. Zorzi, P. Belluttil, M. Boscardin and G. Soncini, IEEE International Conference on Microelectronic Test Structures, Cork, Ireland, IEEE, 2002, pp. 217–222.
15 A. Armin, R. D. J. Vuuren, N. Kopidakis, P. L. Burn and P. Meredith, *Nat. Commun.*, 2015, **6**, 6343.
16 N. Strobel, N. Droseros, W. Köntges, M. Seiberlich, M. Pietsch, S. Schlisske, F. Lindheimer, R. R. Schröder, U. Lemmer, M. Pfannmöller, N. Banerji and G. Hernandez-Sosa, *Adv. Mater.*, 2020, **32**, 1908258.
17 J. Cong, D. Yan, J. Tang, W. Guo and X. Mao, *IEEE Photonics Technol. Lett.*, 2019, **31**, 1979–1982.
18 R. Lukac and K. N. Plataniotis, *IEEE Trans. Consum. Electron.*, 2005, **51**, 1260–1267.
19 K. Kumar, H. Duan, R. S. Hegde, S. C. W. Koh, J. N. Wei and J. K. W. Yang, *Nat. Nanotechnol.*, 2012, **7**, 557–561.
20 T. Jaaskelainen and S. Toyooka, *Opt. Commun.*, 1989, **71**, 133–137.
21 C. Palmer and E. Loewen, *Diffraction grating handbook*, 2005.
22 R. F. Wolffenbuttel, *IEEE Trans. Instrum. Meas.*, 2004, **53**, 197–202.
23 H. Sun, W. Tian, X. Wang, K. Deng, J. Xiong and L. Li, *Adv. Mater.*, 2020, **32**, 1908108.
24 Z. Yang, T. Albrow-Owen, H. Cui, J. Alexander-Webber, F. Gu, X. Wang, T.-C. Wu, M. Zhuge, C. Williams, P. Wang, A. V. Zayats, W. Cai, L. Dai, S. Hofmann, M. Overend, L. Tong, Q. Yang, Z. Sun and T. Hasan, *Science*, 2019, **365**, 1017–1020.
25 A. Polzer, W. Gaberl and H. Zimmermann, *Electron. Lett.*, 2011, **47**, 614–615.
26 C. Xie, L. Zeng, Z. Zhang, Y.-H. Tsang, L. Luo and J.-H. Lee, *Nanoscale*, 2018, **10**, 15285–15293.
27 M. S. Shawkat, H.-S. Chung, D. Dev, S. Das, T. Roy and Y. Jung, *ACS Appl. Mater. Interfaces*, 2019, **11**, 27251–27258.
28 M. O'Brien, N. McEvoy, C. Motta, J.-Y. Zheng, N. C. Berner, J. Kotakoski, K. Elibol, T. J. Pennycook, J. C. Meyer, C. Yim, M. Abid, T. Hallam, J. F. Donegan, S. Sanvito and G. S. Duesberg, *2D Mater.*, 2016, **3**, 021004.
29 Y. Yang, S. K. Jang, H. Choi, J. Xu and S. Lee, *Nanoscale*, 2019, **11**, 21068–21073.
30 L. Ansari, S. Monaghan, N. McEvoy, C. Ó. Coileáin, C. P. Cullen, J. Lin, R. Siris, T. Stimpel-Lindner, K. F. Burke, G. Mirabelli, R. Duffy, E. Caruso, R. E. Nagle, G. S. Duesberg, P. K. Hurley and F. Gity, *2D Mater.*, 2019, **3**, 33.
31 Z.-X. Zhang, L.-H. Zeng, X.-W. Tong, Y. Gao, C. Xie, Y. H. Tsang, L.-B. Luo and Y.-C. Wu, *J. Phys. Chem. Lett.*, 2018, **9**, 1185–1194.

32 S. M. Sze and K. K. Ng, *Physics of Semiconductor Devices*, 2006.

33 Y. Wang, K. Ding, B. Sun, S.-T. Lee and J. Jie, *Nano Res.*, 2016, **9**, 72–93.

34 C. Xie, Y. Wang, Z.-X. Zhang, D. Wang and L.-B. Luo, *Nano Today*, 2018, **19**, 41–83.

35 C.-Y. Wu, J.-W. Kang, B. Wang, H.-N. Zhu, Z.-J. Li, S.-R. Chen, L. Wang, W.-H. Yang, C. Xie and L.-B. Luo, *J. Mater. Chem. C*, 2019, **7**, 11532–11539.

36 Y. Xu, Y. Ma, Y. Yu, S. Chen, Y. Chang, X. Chen and G. Xu, *Nanotechnology*, 2021, **32**, 075201.

37 J.-M. Choi, H. Y. Jang, A. R. Kim, J.-D. Kwon, B. Cho, M. H. Park and Y. Kim, *Nanoscale*, 2020, **13**, 672–680.

38 L. Wang, H. Luo, H. Zuo, J. Tao, Y. Yu, X. Yang, M. Wang, J. Hu, C. Xie, D. Wu and L. Luo, *IEEE Trans. Electron Devices*, 2020, **67**, 3211–3214.

39 C. Xie, X. Zhang, K. Ruan, Z. Shao, S. S. Dhaliwal, L. Wang, Q. Zhang, X. Zhang and J. Jie, *J. Mater. Chem. A*, 2013, **1**, 15348–15354.

40 A. Polzer, W. Gaberl, M. Davidovic and H. Zimmermann, *IEEE SENSORS 1937-1940*, IEEE, Limerick, Ireland, 2011.

41 M. S. Shawkat, J. Gil, S. S. Han, T.-J. Ko, M. Wang, D. Dev, J. Kwon, G.-H. Lee, K. H. Oh, H.-S. Chung, T. Roy, Y. J. Jung and Y. Jung, *ACS Appl. Mater. Interfaces*, 2020, **12**, 14341–14351.

42 A. Ciarrocchi, Ahmet Avsar, D. Ovchinnikov and A. Kis, *Nat. Commun.*, 2018, **9**, 919.

43 E. Okogbue, S. S. Han, T.-J. Ko, H.-S. Chung, J. Ma, M. S. Shawkat, J. H. Kim, J. H. Kim, E. Ji, K. H. Oh, L. Zhai, G.-H. Lee and Y. Jung, *Nano Lett.*, 2019, **19**, 7598–7607.

44 Y. Zhao, J. Qiao, Z. Yu, P. Yu, K. Xu, S. P. Lau, W. Zhou, Z. Liu, X. Wang, W. Ji and Y. Chai, *Adv. Mater.*, 2017, **29**, 1604230.